

Date of publication xxxx 00, 0000, date of current version xxxx 00, 0000.

Digital Object Identifier

# Time-Gating Technique for Recreating Complex Scenarios in 5G Systems

Alejandro Ramírez-Arroyo<sup>1</sup>, Antonio Alex-Amor<sup>1,2</sup>, Carmelo García-García<sup>1</sup>, Ángel Palomares-Caballero<sup>1</sup>, Pablo Padilla<sup>1</sup>, and Juan Valenzuela-Valdés<sup>1</sup>

<sup>1</sup>Department of Signal Theory, Telematics and Communications, Universidad de Granada, Granada 18071, Spain

<sup>2</sup>Information Processing and Telecommunications Center, Universidad Politécnica de Madrid, Madrid 28040, Spain

Corresponding author: Alejandro Ramírez-Arroyo (e-mail: alera@ugr.es).

This work was supported in part by the Spanish Program of Research, Development and Innovation under Project TIN2016-75097-P, Project RTI2018-102002-A-I00 and, Project EQC2018-004988-P, in part by “Junta de Andalucía” under Project B-TIC-402-UGR18 and Project P18.RT.4830 and in part by the predoctoral grants FPU19/01251 and FPU18/01965.

**ABSTRACT** This article presents a novel application of the time-gating technique to the field of propagation channel study. The time-gating technique is well known in the field of antenna measurement and it is used to eliminate reflected components in outdoor measurements or anechoic chambers. In this article, we present a new measurement configuration for shielded chambers that allows to configure different propagation scenarios. In this configuration, the chamber is covered in one part with absorbers and in the other without absorbers (in order to generate reflected components). Applying the time-gating technique, we can modify, adjust and tune the reflections that a certain propagation environment has. This yields a relative control of the propagation environment in both far field and near field regions and allows to quantify the spectral efficiency and signal correlation that MIMO systems would display operating in those propagation environments.

**INDEX TERMS** Anechoic chamber, impulse response, MIMO, recreate scenarios, reverberation chamber, time-gating.

## I. INTRODUCTION

Advances in communication systems and technologies are having a fundamental and profound impact on people's daily lives and social activities [1], [2], leading to a continuous expansion of data traffic and the number of connections [3]. In this scenario, wireless communication systems have become one of the most powerful, dynamic and promising areas for user access to the Information and Communication Technologies (ICTs). The 3rd Generation Partnership Project (3GPP) divides the 5G program into two phases, phase 1 in the Release-15 and phase 2 in the Release-16 [4]. In the first one there is a growing support to vertical industries [5], [6]: non terrestrial networks (NTN), vehicle to all (V2X), public safety, Industrial Internet of Things (IIoT) that has been boosted in the Release-16 and in the predefinition of the Release-17 [7]. Since communication needs will not be fully met by 5G networks, the International Telecommunications Union (ITU) has already set up a working group to look at the development of future networks beyond 5G (ITU-T Focus Group

Technologies for Network 2030, FG NET-2030). This focus group has stated that autonomous vehicles, machine-to-machine mass communications, touch Internet and holographic communications will become a reality in the coming years and frequency bands above 100 GHz will need to be explored in order to make these communications a reality. In this context, any communication system is conditioned and limited by the propagation environment in which the communication takes place [8]. This makes it essential that the influence of the radio environment is properly studied in order to determine the conditions under which the communications take place (level of available power, maximum transmission speed, etc.), as well as the main limitations and clear risks of communication failure. On this basis, many scenarios need to be emulated, such as: Microcellular outdoor scenarios (O2O, Outdoor-to-Outdoor) [9], indoor scenarios [10] (I2I, Indoor-to-Indoor), outdoor-to-indoor scenarios [11], [12] (O2I, Outdoor-to-Indoor), or vehicular scenarios (V2X, Vehicular-to-Vehicular/Infrastructure), among others. Moreover, it will also be necessary to characterize particular scenarios, such

as tunnels, factories, trains and car interior (on-car), which complete the environments proposed for 5G and beyond applications [13], [14]. Therefore, it is necessary to characterize the propagation conditions in a large number of scenarios.

There are many research groups performing in-situ measurements with different channel sounders at different frequencies and very different locations. As an example, three surveys of the propagation measurements can be found in [15]-[17]. However, a cheaper alternative is to reproduce such environments in the laboratory. Different alternatives have been proposed in recent years to perform Over the air Test (OTA) measurements in the laboratory [18]-[22]. The first alternative is to perform measurements in an anechoic chamber with multiple antennas positioned in a circle that are connected to a channel emulator that reproduces the channel conditions. Another cheaper solution is based on reverberation chambers in which the configuration of the scenario is achieved by introducing different objects inside the chamber [23]. For example, in [24] the propagation environment of an oil refinery is compared to the introduction of a certain load into the chamber. In [25], [26] different scenarios are emulated with different angles of arrival and different number of multipath components (MPCs). In addition, there are specific designs to reproduce certain scenarios such as those found in [27], [28] where vehicle scenarios are reproduced. In order to refine those scenario emulations, post-processing techniques have been developed, such as changing the Rician factor [29] or selecting certain samples [30] to reproduce a specific scenario. In order to increase the number of recreated scenarios, this article proposes the use of a scenario creation strategy based on the well-known time-gating technique for measuring antennas, where different parameters such as spectral efficiency, signal correlation or power balance are analyzed. On what follows, it is shown how the time-gating technique can be used to modify the real propagation scenario allowing to remove some reflections inside a chamber, or with an appropriate signal processing, to change the time of arrival of some reflections. Furthermore, it allows to go beyond the limits of a certain measurement setup, i.e., allowing new degrees of freedom with the creation of artificial reflections.

The paper is organized as follows. Section II introduces the time-gating technique and particularizes its use to antenna measurement. Sections III and IV show the capabilities of the time-gating technique for the recreation of complex scenarios in anechoic chambers and reverberation chambers, respectively. Finally, the main conclusions of the work are drawn in Section V.

## II. MEASUREMENT SET-UP AND TIME-GATING TECHNIQUE

This section describes the measurement set-up and the steps followed in the application of the time-gating technique. Afterwards, we particularize its use to the characterization of antenna radiation patterns, in order to test the capabilities of the method.

The measurements were taken in a shielded chamber with the following dimensions: 5x3.5x3.5 meters. This chamber was designed to make measurements above 10 GHz, so we will have a maximum wavelength of 3 cm. Specifically, in this article measurements above 30 GHz have been made. Therefore, a maximum wavelength of 1 cm is considered, which together with an antenna diameter of 28 mm (see Section III), ensures that measurements are in the far field. This assumption is valid due to the use of virtual arrays for the considered MIMO configurations. The chamber, shown in Figs. 1 and 2, is divided into two parts. The left part resembles a traditional anechoic chamber and has been successfully used for the measurement of radiation patterns in [31]-[33]. The measurement of radiation patterns is possible because the minimum reflections caused in the reverberant chamber can be eliminated with the time-gating technique and because the level of the reflections is very low when going through an electrically long distance (large number of wavelengths), since they are reflected in some of the walls on the right. The part on the right has been left uncovered with absorbers to resemble a reverberation chamber. If we position the transmitter in the direction of the wall there will be multiple reflections that will vary depending on the direction. In this way we can approximately control the number of reflections that our measurement has. The chamber is equipped with two different positioning systems. On one side a motorized system has been installed that allows the movement of the receiving antenna in the  $x$ -axis and in the  $z$ -axis according to Fig. 3, with a movement amplitude of 2 meters in the  $x$ -axis and 1 meter in the  $y$ -axis with the aim of being able to form virtual arrays. On the other side we have a motorized table that allows us to move in 4 directions: (i) the 360° turn in roll ( $\beta$ ) as shown in Fig. 1 (ii) the turn in azimuth ( $\phi$ ), (iii) the movement in  $x_2$ -axis, that is in parallel with the  $x$ -axis of the other system and (iv) the movement in  $y$ -axis (Fig. 3) to move the two systems closer and further apart. Therefore, at this end it will be possible to configure virtual arrays with almost infinite possibilities. Depending on the configuration and the pointing direction, it will allow us to have a relative control of the directions of arrival and the number of clusters. From now and on, we will refer in this article to the left side as the anechoic chamber part and to the right side as the reverberant chamber part although strictly speaking they are neither an anechoic nor a reverberant chamber.

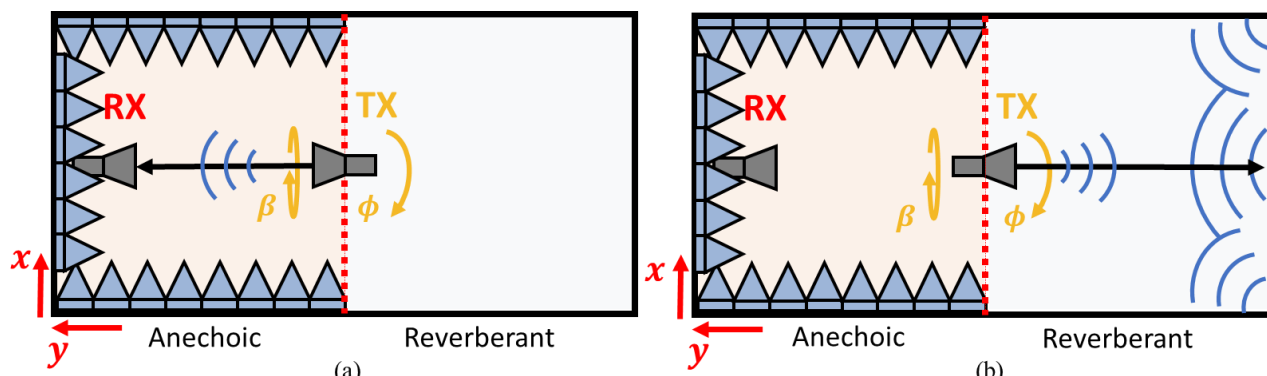


FIGURE 1. Schematics of the anechoic (a) and reverberation (b) chamber. In the anechoic chamber, the receiver is reached by LoS to the transmitter. In the reverberation chamber, the receiver is reached by multiple paths due to the multiple reflections.



FIGURE 2. Panoramic view of the chamber. The picture is taken from the bottom right of the diagrams view.

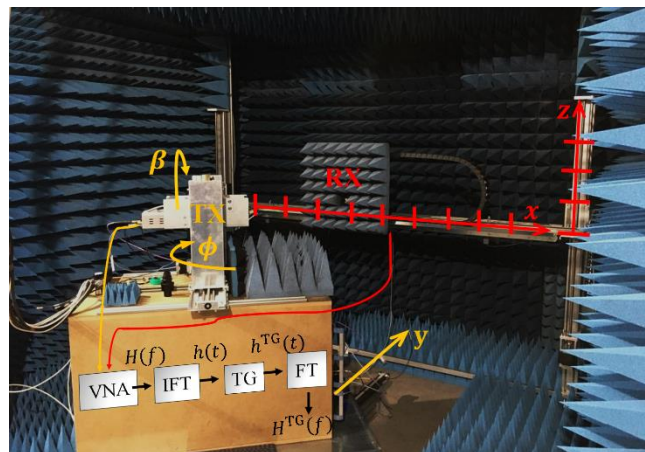


FIGURE 3. Antenna measurement scenario and signal processing steps. The transmitter (TX) antenna is able to move in roll ( $\beta$ ) and azimuth ( $\phi$ ) angles and along the  $y$  axis. The receiver (RX) antenna is able to move along the  $x$  and  $z$  axes.

Figs. 1(a) and 1(b) show a sketch of the anechoic and reverberant chamber, respectively. Fig. 2 illustrates a panoramic view of the chamber. The transmitter can be rotated to target the anechoic zone or the reverberant zone. This transmitter can be oriented on three axes ( $y$ ,  $\phi$ ,  $\beta$ ) as Fig. 3 details. Also, the receiver has mobility in the axes  $x$  and  $z$ . Fig. 3 shows the signal processing steps associated to the time-gating technique. The frequency samples acquired in the VNA represent the channel matrix  $H(f)$ . The time-gating technique enables the channel matrix processing by means of controlling the impulse response of the channel  $h(t)$ . In a first step,  $h(t)$  is obtained from  $H(f)$  after applying the inverse Fourier transform (IFT). Then, the impulse response  $h(t)$  is modified according to the needs of the scenario: In antenna measurement, noise and reflections are removed from the radiation pattern. In propagation, we may want to amplify or create artificial reflections, in order to study their impact on the capacity of the channel. Finally, the modified channel matrix  $H^{TG}(f)$  is recovered from the time-gated impulse response  $h^{TG}(t)$  with the use of the Fourier transform (FT). This  $H^{TG}(f)$  is the new channel matrix that can recreate new scenarios. We are interested in applying the time-gating technique for the recreation of realistic propagation scenarios. However, time-gating has also application in antenna measurement [34], being particularly useful to improve the performance of imperfect

anechoic environments. In addition, its use has recently been extended for the accurate characterization of antenna radiation patterns in reverberating enclosures [35]. In our case, it will be our test field in order to validate the time-gating method and calibrate the optimal parameters of its configuration and it is depicted in Appendix A.

### III. RECREATING SCENARIOS IN ANECHOIC CHAMBERS

In this section, the potential of the time-gating technique for the recreation of MIMO scenarios inside anechoic chambers is illustrated. In this side of the chamber the environments are fully controlled and it serves us to test and validate our technique. The objective of this section is to show that with a single measurement (SISO) we can recreate several scenarios and save some resources and measurements. In Appendix B, it is described the method used to estimate the time of arrival and the amplitude of the reproduced arrays.

#### A. MISO SCENARIO

As an example, we will try to recreate with the use of time-gating the measurement scenario presented in Fig. 4. Four transmitting antennas are separated by 30 cm forming

a linear array. The RX antenna is placed at 80 cm from the first TX antenna, TX<sub>1</sub>. All radiating elements are standard gain horns, fed in this case with a WR22 waveguide-to-coaxial transition. The operating frequency range of the measurement covers from 32 GHz to 39 GHz.

The normalized impulse response  $h(t)$  of the measured MISO (Multiple Input Single Output) scenario is illustrated in Fig. 5(a). For the sake of clarity, the peaks associated to the different TX antennas are marked in different colors. The location of the peaks is related to the distance between TX and RX antennas. The first transmitting antenna (TX<sub>1</sub>) is located at 80 cm from the RX antenna. As a consequence, the propagating signal takes 2.67 ns to reach the RX antenna. However, note that the maximum is located at 3.4 ns, taking into account the length of the waveguide-to-coaxial transitions, not included in the calibration. The separation between consecutive peaks is constant in Fig. 5(a), being approximately 1 ns, since the distance between adjacent antennas is constant too. Therefore, the impulse responses of TX<sub>2</sub>, TX<sub>3</sub>, and TX<sub>4</sub> are centered at 4.4 ns, 5.4 ns and 6.4 ns, respectively. Additionally, if reflections and noise are negligible in the measurement, the amplitude decay between consecutive peaks can be approximated by only considering free space losses. The attenuation factor  $att$  is estimated for each TX<sub>*i*</sub> antenna as the relation between the distances of the considered TX<sub>*i*</sub> antenna and the first transmitter antenna TX<sub>1</sub> to the RX antenna. That is, 80cm/80cm=1 for TX<sub>1</sub>, 80cm/110cm=0.73 for TX<sub>2</sub>, 80cm/140cm=0.58 for TX<sub>3</sub> and 80cm/170cm=0.47 for TX<sub>4</sub>.

As a result, the measured impulse response of the complete MISO scenario can be reconstructed from the impulse response of an individual TX antenna. For this case, we applied the time-gating technique over TX<sub>1</sub> and kept the relevant information of the measurement (from 1.8 ns to 5 ns). A symmetric Hann window with a relative window size of 20% is used in the process. Then, identical but attenuated and delayed copies of TX<sub>1</sub> are used to recreate the impulse responses of TX<sub>2</sub> ( $att = -0.73$ ,  $t_{TX_2} = 4.4$  ns), TX<sub>3</sub> ( $att = 0.58$ ,  $t_{TX_2} = 5.4$  ns) and TX<sub>4</sub> ( $att = -0.47$ ,  $t_{TX_4} = 6.4$  ns). For TX<sub>2</sub> and TX<sub>4</sub>, note that a minus sign was used in the attenuation factor since the TX antennas are separated by half a wavelength. Thus, this sign preserves the original shape of the impulse response in Fig. 5(a) by adding an additional phase of 180°.

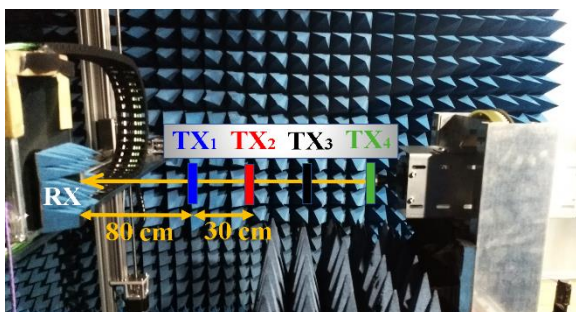


FIGURE 4. Measurement scenario for the MISO (4x1) system. The TX antennas are separated by 30 cm, forming a virtual linear array.

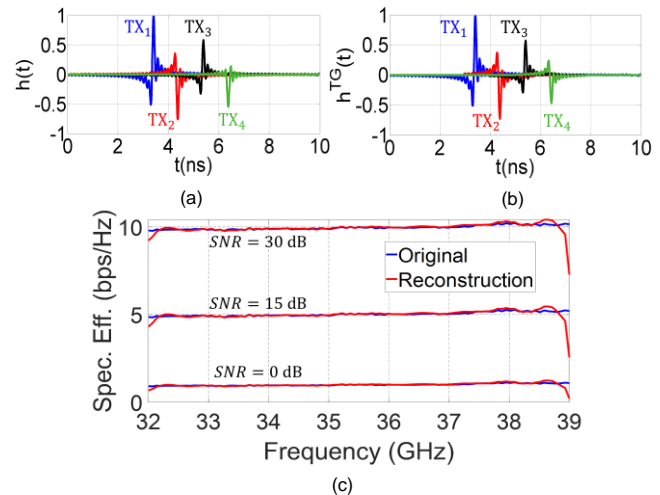


FIGURE 5. Normalized impulse response of the MISO scenario: (a) original, (b) reconstructed with time-gating technique. (c) Spectral efficiency for different SNR values.

Fig. 5(b) presents the reconstructed impulse response of the MISO scenario after the time-gating technique is applied. As it is shown, the similarities between the original and reconstructed impulse response of Figs. 5(a) and 5(b) are noticeable.

In order to quantify the quality of the recreation, we will compare the spectral efficiency of the original and recreated scenarios. The spectral efficiency of a MIMO (Multiple Input Multiple Output) system is calculated according to [36]

$$\eta \left[ \frac{\text{bps}}{\text{Hz}} \right] = \log_2 \left| \det \left( \mathbf{I}_{N_{RX}} + \frac{SNR}{N_{TX}} \mathbf{H}^H \mathbf{H} \right) \right| \quad (1)$$

where  $N_{TX}$  is the number of transmitter antennas,  $N_{RX}$  is the number of receiver antennas,  $SNR$  is the signal-to-noise ratio,  $\mathbf{H}$  is the channel matrix of dimensions  $N_{TX} \times N_{RX}$ , and the superscript  $H$  indicates the conjugate transpose. To include the frequency dependence of the channel, channel matrices  $\mathbf{H}$  are normalized as detailed in [37], [38]

$$\mathbf{H}_{\text{norm}}(f_i) = \mathbf{H}(f_i) \left[ \frac{1}{N_f} \sum_{i=1}^{N_f} \|\mathbf{H}(f_i)\|^2 \right]^{-1/2} \quad (2)$$

where  $\|\cdot\|$  is the Frobenius norm.

Fig. 5(c) shows the spectral efficiency of the original (measured) and reconstructed scenarios for different SNR values. As it can be appreciated, there is an excellent agreement between both curves. The differences at the beginning and end of the frequency band are caused by the frequency window used in the Fourier transform. With the use of the time-gating technique, it is shown how the original MISO scenario can be recreated from the measurement of a single TX antenna, saving time and resources during the process. This technique could be of special interest for massive MIMO scenarios, due to their complexity and large number of elements required.

## B. MIMO SCENARIO

Fig. 6 presents the measurement scenario of a MIMO 4x3 system. Four transmitter antennas are separated by 30 cm along the  $y$  axis and three receiver antennas are separated by 40 cm along the  $x$  axis. We will demonstrate that the time-gating technique can be used to recreate MIMO scenarios, simplifying and saving resources in the process. Similarly to the previous study, the measured impulse response of the complete MIMO channel can be reconstructed from the impulse response of a reference SISO scenario. Thus, the channel matrix ( $4 \times 3$ ) is formed by attenuated and delayed copies of the reference signal,  $h_{ref}(t)$ . In our case, the reference TX and RX antennas from which the copies are built are TX<sub>1</sub> and RX<sub>2</sub>, respectively. The attenuation factors and time delays are subsequently extracted by applying basic trigonometry and taking into account the gain drop associated to the radiation properties of the utilized horn antennas. More details are provided in Appendix B.

Fig. 7 illustrates the original and reconstructed spectral efficiency as a function of the SNR for different scenarios: MISO 4x1 (all TX and RX<sub>2</sub>), MIMO 4x2 (all TX, RX<sub>1</sub> and RX<sub>2</sub>), and MIMO 4x3 (all TX and all RX). In addition, the theoretical limit is shown, where a fully uncorrelated matrix is generated by using a normal Gaussian distribution. In this case, all the signals between any transmitter and receiver are completely different, which maximizes the transmitted information and consequently, the spectral efficiency. Analyzing the results, a noticeable agreement is evidenced between the measured and reconstructed scenario. As expected, the spectral efficiency increases as the SNR and the number of receivers is increased. However, note that the increase in spectral efficiency between MISO and MIMO 4x2 systems is greater than between MIMO 4x2 and MIMO 4x3. This fact could be linked to the high correlation [39] between the signals arriving at RX<sub>1</sub> and RX<sub>3</sub>. For this reason, Fig. 8 shows the correlation matrices of the RX antennas for the configuration illustrated in Fig. 6. In the recreated scenario, the signals arriving at RX<sub>1</sub> and RX<sub>3</sub> are forced to be identical due to the symmetry of the scenario (see Appendix B). Thus, the correlation coefficients  $C_{13} = C_{31}$  are exactly one in Fig. 8(a). In the original measured scenario, these coefficients are expected to be

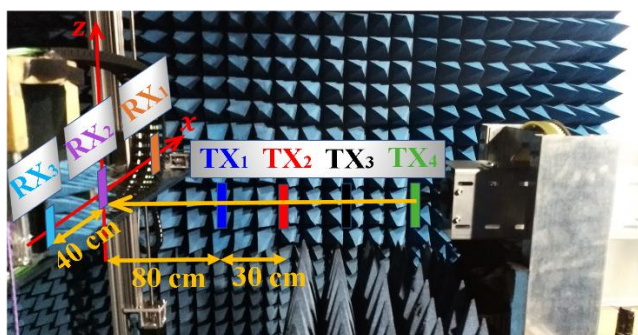


FIGURE 6. Measurement scenario for the MIMO (4x3) system. TX antennas are separated by 30 cm. RX antennas are separated by 40 cm.

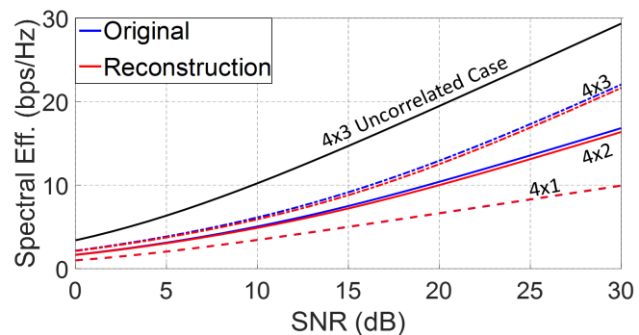


FIGURE 7. Original (blue curves), reconstructed (red curves) and theoretical limit (black curve) spectral efficiencies for different MIMO  $N_{TX} \times N_{RX}$  systems when varying the number of RX antennas. For each SNR value, the spectral efficiency is averaged in the whole frequency range.

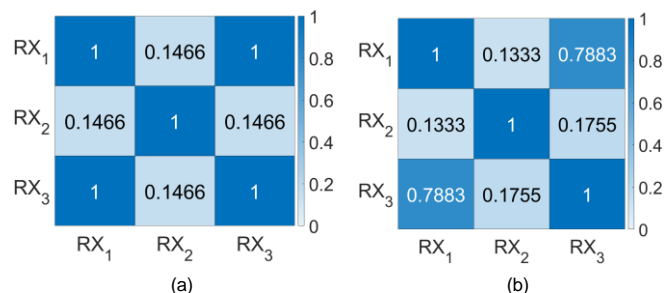


FIGURE 8. Correlation matrices of the three RX antennas for the (a) reconstructed and (b) original scenarios.

high, but different from one due to asymmetries in the radiation pattern, reflections, noise, etc. Conversely, the receivers RX<sub>1</sub> and RX<sub>3</sub> are uncorrelated with the central receiver RX<sub>2</sub>, as the coefficients  $C_{12} = C_{21}$  and  $C_{23} = C_{32}$  indicate in Figs. 8(a) and 8(b).

Fig. 9 focuses on the MIMO 4x2 system for every possible combination of RX antennas. The lowest spectral efficiency is obtained for RX<sub>1</sub> and RX<sub>3</sub> due to the high correlation between the receivers (see Fig. 8(b)). When the system is measured with RX<sub>1</sub> and RX<sub>2</sub>, or RX<sub>2</sub> and RX<sub>3</sub>, the spectral efficiency is higher than the previous case on account of the decorrelation of the signals. In fact, the spectral efficiency when RX<sub>1</sub>-RX<sub>2</sub> are used is slightly higher since the correlation in this case is slightly lower than in the case of RX<sub>2</sub>-RX<sub>3</sub>.

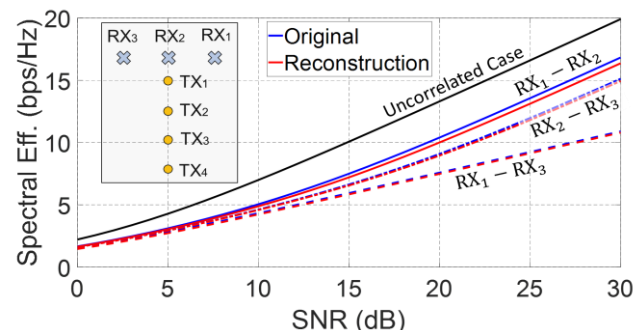


FIGURE 9. Original (blue curves), reconstructed (red curves) and theoretical limit (black curve) spectral efficiencies for every possible combinations of RX antennas in a MIMO 4x2 system. For each SNR value, the spectral efficiency is averaged in the whole frequency range. Solid (—), dash-dotted (— · —) and dashed (---) lines correspond to RX<sub>1</sub> - RX<sub>2</sub>, RX<sub>2</sub> - RX<sub>3</sub> and RX<sub>1</sub> - RX<sub>3</sub> pairs of RX antennas, respectively.

The measurements on the MIMO 4x2 system can also be compared with the theoretical limit. Compared to the MIMO 4x3 system (see Fig. 7), the measurements in Fig. 9 are closer to the theoretical limit. This fact is explained because in the MIMO 4x2 system it is possible to decorrelate the signals received as explained previously. In the MIMO 4x3 system the correlation between  $RX_1$  and  $RX_3$  is always taken into account, and due to the symmetry of the system the correlation is close to one, moving the measurement away from the theoretical limit.

#### IV. RECREATING SCENARIOS IN REVERBERATION CHAMBERS

##### A. SISO SCENARIO

In this section, we show how the time-gating technique can be applied for the recreation of complex scenarios in reverberation chambers. For this case, the measurement scenario is presented in Fig. 10. A transmitter horn antenna (same one used in Section III) points at the metallic wall of the reverberation chamber. The multiple reflections inside the reverberating environment are acquired by a receiver antenna, which is aligned with the TX antenna. The frequency range of the measurement is set from 38 GHz to 39 GHz.

Fig. 11 shows the original and reconstructed signals inside the reverberation chamber. As previously done, we will use the spectral efficiency to quantify the quality of the recreation. It is remarkable that fewer reflections are observed compared to a reverberant chamber. It is due to the fact that half of the chamber is anechoic, so some of the reflections are attenuated. The reconstruction process is presented in three steps: Fig. 11(a) illustrates a comparison between the original and reconstructed scenarios when only the primary reflection  $R_p$  is considered. As it can be appreciated, the primary reflection, placed at 22 ns, contains most of the relevant information about the original

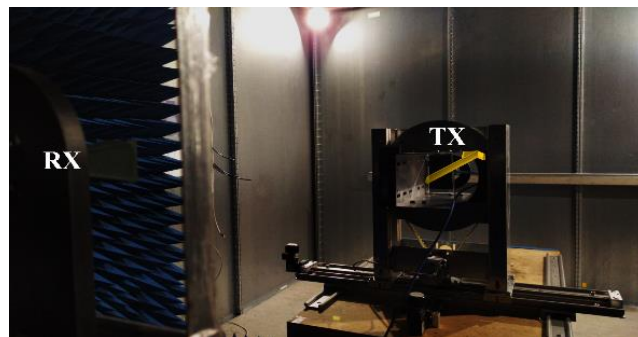


FIGURE 10. Measurement scenario for the SISO system inside the reverberation chamber. A transmitter antenna (TX) points at the metallic wall of the chamber and a receiver antenna (RX) acquires the multiple reflections inside it.

scenario. It gives an average estimation of the spectral efficiency. However, secondary reflections must be also considered to completely define the scenario. Thus, identical but attenuated and delayed copies of  $R_p$  are used to recreate the secondary reflections  $R_{s1}$  and  $R_{s2}$ . In the present scenario,  $R_{s2}$  has a higher amplitude than  $R_{s1}$ . Therefore, the contribution of  $R_{s2}$  to the spectral efficiency is expected to be more significant compared to  $R_{s1}$ . Fig. 11(b) confirms this fact, showing that a good recreation of the measured scenario can be achieved by only considering the primary reflection  $R_p$  and the second secondary reflection  $R_{s2}$ . Finally, Fig. 11(c) presents the final reconstruction, which considers the primary reflection  $R_p$  and the two secondary reflections  $R_{s1}$  and  $R_{s2}$ . The inclusion of  $R_{s1}$  in the recreation adjusts some of the small details of the small measured spectral efficiency. The improvement through the addition of reflections can be quantified from the spectral efficiency normalized mean square errors (NMSEs), which for Figs. 11(a), 11(b) and 11(c) are 2.164, 1.653 and 1.506 respectively. The greater contribution of  $R_{s2}$  with respect to  $R_{s1}$  implies a greater decrease in the NMSE between Figs. 11(a) and 11(b) than

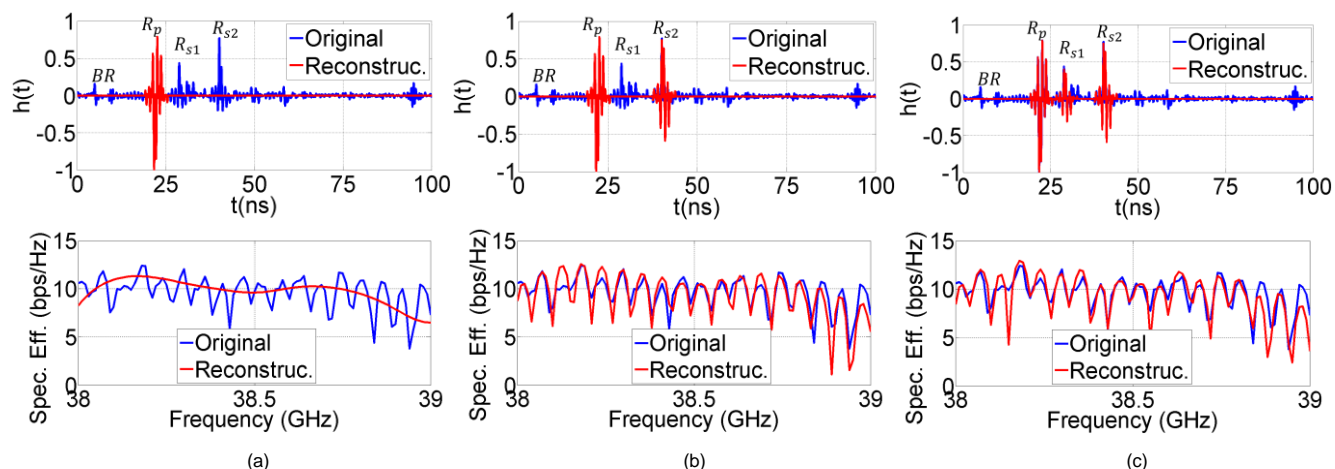
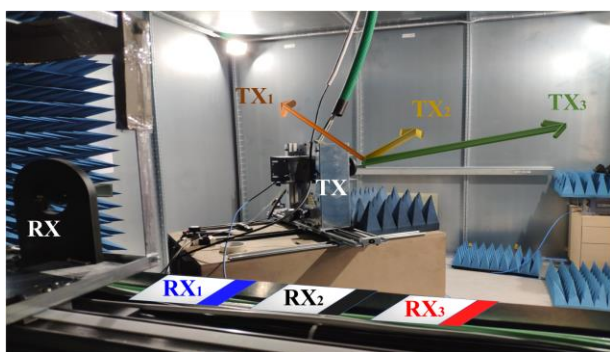


FIGURE 11. Original and reconstructed signals in the reverberation chamber. The reconstruction is presented in three steps, and the impulse responses and spectral efficiencies (for a  $SNR = 30$  dB) are provided together: (a) Only the primary reflection ( $R_p$ ) is considered. (b) The primary reflection ( $R_p$ ) and the second secondary reflection ( $R_{s2}$ ) are considered. (c) Final reconstruction, including the primary reflection ( $R_p$ ) and both secondary reflections ( $R_{s1}, R_{s2}$ ). Secondary reflections are identical but attenuated and delayed copies of  $R_p$  ( $R_{s2} = -0.4R_p$ ,  $R_{s1} = -0.75R_p$ ). BR refers to back radiation. The spectral efficiency NMSEs for the three reconstructions are 2.164, 1.653 and 1.506, respectively.

between Figs. 11(b) and 11(c). The rest of the peaks observed in the measured impulse response of Fig. 11 are low-amplitude reflections that contain little information about the environment. Therefore, these peaks were excluded from the recreation for the sake of simplicity. Conversely, the origin of the two peaks observed at 5 ns and 9.5 ns is different. They appear before the primary reflection. This means that both peaks correspond to back radiation (*BR*) from the TX antenna. In addition, the amplitude level of both peaks is reduced, since the transmitter horn antenna is a directive antenna with low back-lobe level. Unlike the flat response observed in the MISO scenario of Fig. 5(c), there is a prominent ripple in the measured spectral efficiency of Fig. 11. The existence of multiple reflections in the reverberation chamber creates interference patterns that cause an increase or decrease in spectral efficiency at certain frequencies. For this reason, the reconstructed spectral efficiency is flatter when only a single reflection,  $R_p$ , is considered (see Fig. 11(a) vs Figs. 11(b) and 11(c)). In addition, the amplitude of the ripple is related to the amplitude of the secondary reflections. That is, the bigger the secondary reflections are, the bigger the ripple is.

## B. MIMO SCENARIO

Once the SISO case has been studied, a more complex case is analyzed. Fig. 12 presents the measurement scenario of the MIMO 3x3 system located inside the reverberation chamber. Three TX antennas, oriented in azimuth angles of  $-45^\circ$ ,  $0^\circ$  and  $45^\circ$ , face the front metallic wall of the reverberation chamber. Three RX antennas, separated by 40 cm, are placed along the  $x$  axis behind the TX antennas. The frequency range of the measurement is set from 36 GHz to 39 GHz.



**FIGURE 12.** Measurement scenario for the MIMO system inside the reverberation chamber. Three transmitter antennas (TX) point at the metallic wall of the chamber and three receiver antennas (RX) acquire the multiple reflections inside it.

Fig. 13 shows the nine original and reconstructed time-domain signals for the different TX and RX antennas. Similar to previous sections, a reference signal ( $TX_2 - RX_2$ ) is used to replicate the different reflections observed in the chamber. The primary reflection is observed approximately at 22 ns, which fits the expected travelling time corresponding to the distance that the wave takes to hit

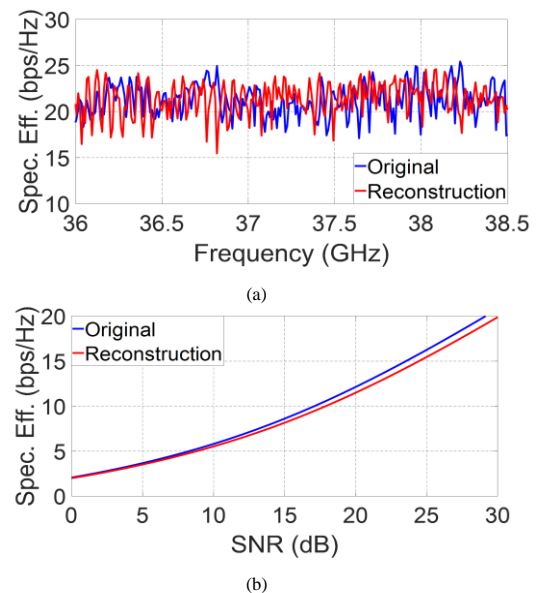


**FIGURE 14.** Original and reconstructed spectral efficiencies for the MIMO 3x3 scenario inside the reverberation chamber: (a) as a function of the frequency (SNR = 30 dB), (b) as a function of the SNR (averaged in frequency).

the front wall and to be reflected back towards the receivers, approximately 6.2 meters. Finally, Fig. 14 shows the original and reconstructed spectral efficiencies as a function of the frequency and SNR. Good agreement is observed in the recreation.

## C. MODIFYING THE MIMO SCENARIO

The time-gating technique allows to recreate complex scenarios, but also to go beyond the limits imposed by the measurement setup. In previous sections, we saw that the phase and amplitude of an antenna array can be easily controlled and that the number of required antennas can be reduced, which is especially useful for massive MIMO systems. Inside reverberation chambers, controlling and modifying the different reflections could be of potential interest. As an example, Figs. 15(a) and 15(b) illustrate the effect of eliminating all reflections inside the chamber except the primary one, located at 22 ns in Fig. 13. Eliminating the reflections in the reverberation chamber provokes an increase in the correlation of the different MIMO channel, as shown in the correlation matrices of Figs. 15(c) and 15(d). As a consequence, the spectral efficiency is reduced.

The decrease in spectral efficiency due to the correlation is not as high as it might be expected, being only 1bps/Hz. Therefore, other factors such as the power balance can be decisive for the spectral efficiency curve. In order to see the effects of the power balance for each TX – RX pair in the MIMO system, Table I is shown. It presents the average power values of each TX – RX pair normalized to the lowest average power. Consequently, the values shown indicate the power factor in which each TX – RX pair multiplies to the worst case.

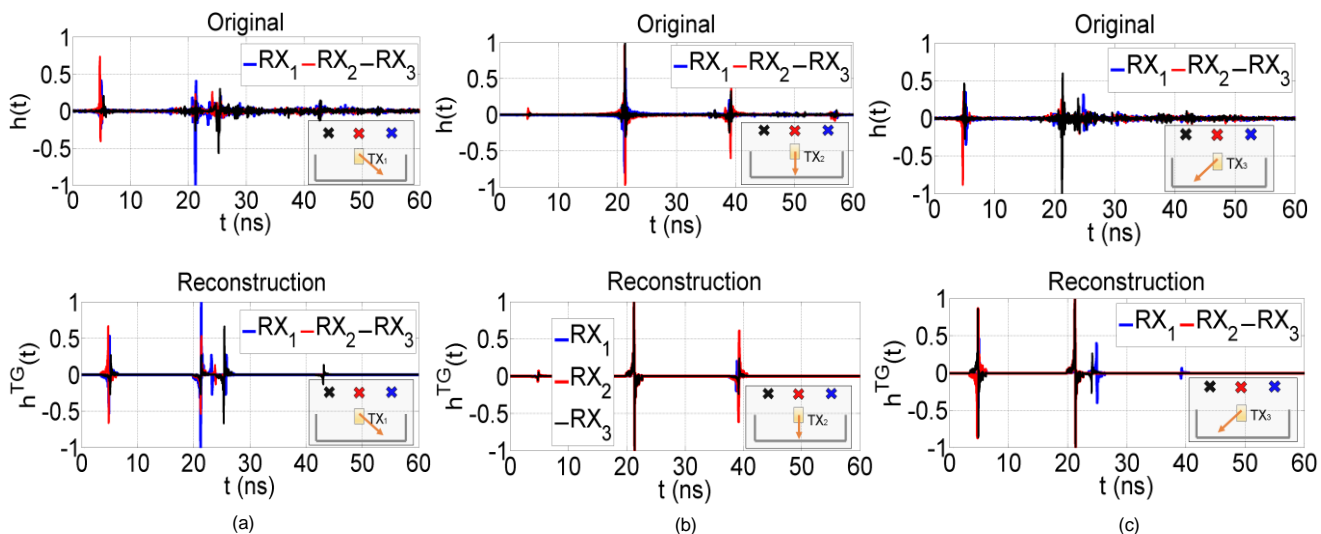
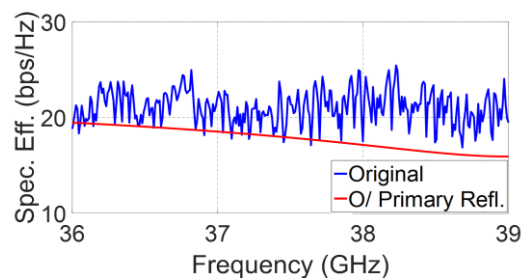


FIGURE 13. Original and reconstructed signals for the MIMO 3x3 scenario inside the reverberation chamber: (a)  $TX_1$  ( $-45^\circ$ ), (b)  $TX_2$  ( $0^\circ$ ), (c)  $TX_3$  ( $45^\circ$ ).

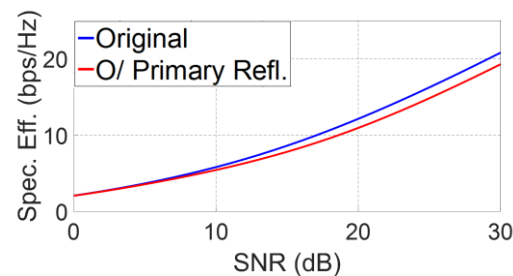
TABLE I  
NORMALIZED AVERAGE POWER VALUES

	$RX_1$	$RX_2$	$RX_3$
$TX_1$	1.60	1.22	1.21
$TX_2$	8.11	11.77	8.69
$TX_3$	1	1.53	1.76

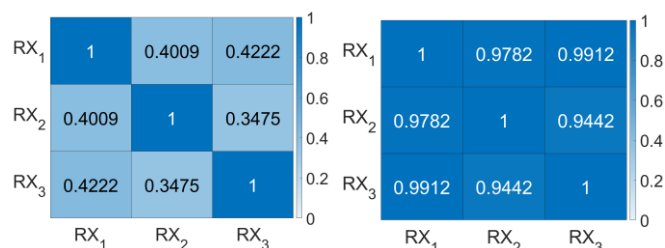
The table shows a clear trend. The pairs involving  $TX_2$  have an average power approximately one order of magnitude higher than the other transmitters. This can be explained by the fact that  $TX_1$  and  $TX_3$  are oriented in azimuth angles of  $-45^\circ$  and  $45^\circ$  respectively. Thus, the distance the wave travels is greater for these transmitters, as well as the number of reflections given the shape of the chamber. The normalized average power values are not exactly identical for  $TX_1$  and  $TX_3$  due to the fact that the reverberant environment is not perfectly symmetrical to the YZ plane. However, these receivers keep the same order of magnitude. The power unbalance causes the real behavior of the system to tend to a 1x3 SIMO rather than a 3x3 MIMO since only one transmitter radiates 77.4% of the power received by the receivers. To solve this problem, the values of each pair are scaled to create a perfectly balanced system. The results are shown in Fig. 16, where the spectral efficiency is shown for the original signal and only for the primary reflection, both in the balanced and unbalanced case. Additionally, the power balance increases the spectral efficiency both for the original signal and for primary reflection. On the other hand, when the power is balanced the effect of signal decorrelation is much greater as the curves are much more separated. Power balance does not change the correlation of the signals, so it remains as shown in Figs. 15(c) and 15(d).



(a)



(b)



(c)

(d)

FIGURE 15. Degradation of the spectral efficiency after removing all reflections in the reverberation chamber except the primary one (red curves): (a) as a function of the frequency (SNR = 30 dB), (b) as a function of the SNR (averaged in frequency). Correlation matrices of the three TX antennas for the (c) original scenario and (d) the modified scenario where only the primary reflection (22 ns) is considered.

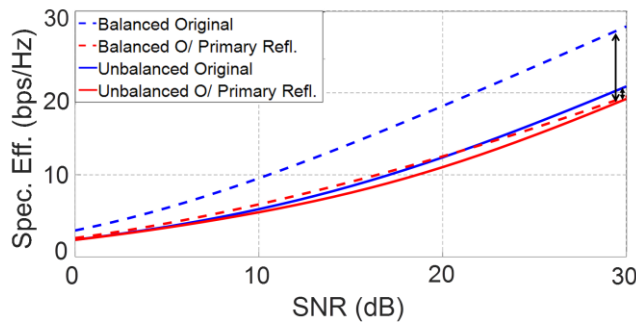


FIGURE 16. Spectral efficiency comparison for balanced and unbalanced power cases for the MIMO scenario in the reverberation chamber.

## V. CONCLUSION

This article presents a deep analysis of the use of the time-gating technique to the field of propagation channel. Several parameters concerning the propagation channel are analyzed, such as spectral efficiency, signal correlation and power balance. The time-gating technique is well known in the field of antenna measurement as a tool to eliminate reflected components in outdoor measurements or imperfect anechoic chambers. This technique can be applied in both far field and near field measurements. Taking advantage of its potential, a new measurement configuration for shielded chambers based on time-gating is provided. This configuration allows to configure different propagation scenarios. The proposed configuration is based on a mixed chamber that is covered in one part with absorbers (anechoic zone) and in the other without absorbers (reverberating zone) in order to generate reflected components. Applying the time-gating technique, it is possible to modify, adjust and tune the reflections that a certain propagation environment has. This yields a relative control of the propagation environment and lets to quantify the capacity that MIMO systems can display operating in those propagation environments. Furthermore, it allows to go beyond the limits of a certain measurement setup, allowing new degrees of freedom with the change of the time of arrival of some reflections or the creation of artificial reflections.

In order to show the potential of the time-gating technique for the recreation of propagation scenarios inside anechoic chambers, different configurations have been deeply studied in the frequency range between 32 GHz and 39 GHz. Therefore, MISO, MIMO and SISO scenarios are recreated either for anechoic or reverberating environment. Additionally, we explore the capability of tune the propagation scenario controlling the phase and amplitude of an antenna array along with modifying the different reflections in the scenario, which is especially useful for massive MIMO systems. The experimental results provided are of relevance and validate the use of the time-gating technique for the recreation and characterization of new propagation channels, reducing the complexity and the limitations derived from the on-site measurements of real

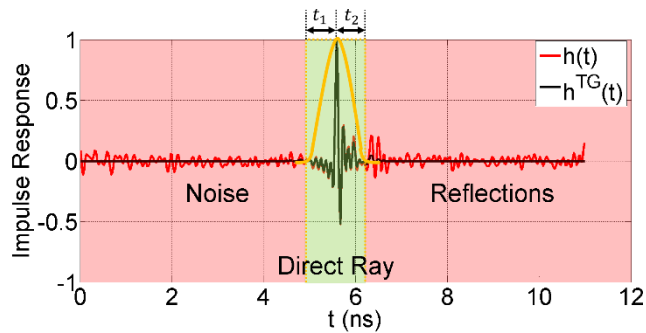
scenarios. As a future direction, several metrics can be exploited when applying time-gating. Some of them, such as the angle and time of arrival, add new degrees of freedom, which add a wide range of possibilities to the recreation of scenarios. Thus, this technique opens the door to create a tool capable of emulating different specific environments (vehicular scenarios, trains, tunnels, etc.) in the laboratory based on measurements in the chamber.

## APPENDIX A. TIME GATING VALIDATION

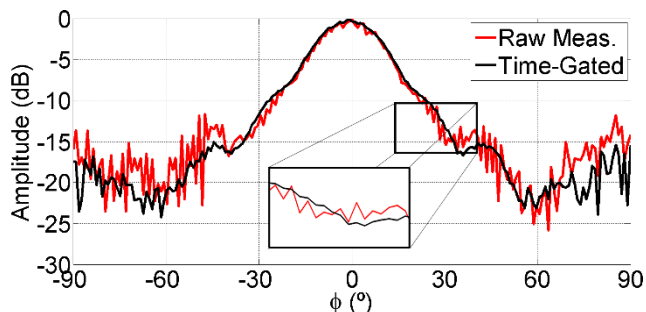
For the validation of the method, we set the following measurement scenario based on the configuration of the anechoic chamber shown in Fig. 3. A fixed receiver antenna is placed in front of a transmitter antenna, which is only able to move in azimuth angles ( $\phi$ ). Both radiating elements are standard gain horns with 47 mm diameter, fed with a WR-34 waveguide-to-coaxial transition. The operation frequencies of the measurement are within the range 22-27.5 GHz. The radiation pattern is measured with a R&S-ZVA67 vector network analyzer (VNA). Note that the pattern results of the UGR measuring system shown in this Appendix have been validated through an exhaustive comparison process with the measuring facilities of the Technical University of Madrid (UPM) [40].

Fig. 17 shows the normalized impulse response of the system before,  $h(t)$ , and after,  $h^{TG}(t)$ , applying the time-gating technique. The time interval associated to the direct ray is highlighted in green in the figure. Outside this interval, the presence of noise and reflections provokes a further degradation in the reconstruction of the antenna radiation pattern. With the time-gating technique, the impulse response is truncated in the interval of interest and noise and reflections are eliminated. As illustrated in Fig. 17, different kind of windows can be applied for this purpose [41].

Fig. 18 presents the radiation pattern of the horn antenna (E-plane) at 27.5 GHz before and after applying the time-gating technique. The bandwidth of the measurement is  $B = 5.5$  GHz, with  $N_f = 101$  frequency samples. Then, a symmetrical-centered time-domain ( $t_1 = t_2 = t_{TG}$ ) Hann window was used for the reconstruction of the radiation pattern. As shown in Fig. 18, the time-gating technique improves considerably the quality of the measurements after eliminating the ripple associated to noise and reflections. Furthermore, it has emphasized the presence of the first null in the radiation pattern ( $\pm 38^\circ$ ), which was masked by reflections in the anechoic chamber. These facts potentially allow to reduce the number of azimuth samples in order to speed up the measurement, while maintaining a good overall performance. We should remark that no additional smoothing process has been utilized in Fig. 17 except from the time-gating itself. As a consequence, the ripple can be further reduced if the time-gated signal is smoothed in a post-processing step (i.e., see Fig. 22).



**FIGURE 17.** Normalized impulse response of the original  $h(t)$  and time-gated  $h^{TG}(t)$  signals. Time-gating is applied in the antenna measurement scenario to eliminate noise and reflections.



**FIGURE 18.** Radiation pattern of the horn antenna (E-plane) at 27.5 GHz before and after using the time-gating technique. For the time-gated measurement, a Hann window was used with  $t_1 = t_2 = t_{TG} = 2.2$  ns (20%). For a fair comparison, no additional smoothing technique has been applied to the time-gated signal in a post-processing step.

### B. EFFECT OF THE WINDOW SIZE

The window size plays a fundamental role in the time-gating technique. Narrow windows may eliminate part of the information about the direct ray contained in the impulse response. Conversely, wide windows may not completely eliminate reflections in the anechoic chamber.

Fig. 19 shows the effect of varying the window size on the radiation pattern when a symmetrical Hann window is applied. In the plot, the width of the window is referred as a percentage of the total time interval (11 ns) of the impulse response. As previously detailed, a narrow window (green curve: 1%) cuts relevant information of the impulse response, leading to the degradation of the main lobe and the loss of the first null in the radiation pattern. Conversely, a wide window (blue curve: 80%) cancels out the beneficial effect of time-gating, since most of the reflections are kept inside the window. For this measurement scenario, we determined that  $t_{TG} = 20\%$  (black curve) is an optimal value.

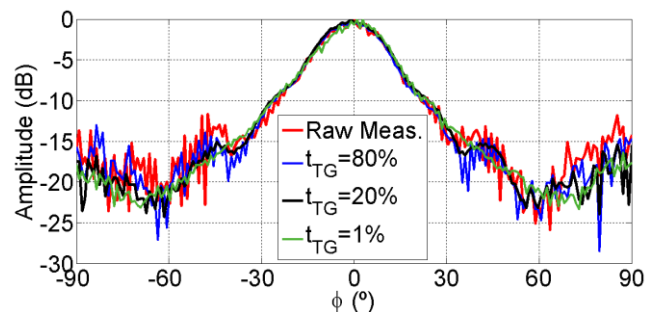


**FIGURE 19.** Effect of varying the window width on the radiation pattern. In the plot,  $t_1 = t_2 = t_{TG}$  is referred as a percentage of the total time (11 ns).

### C. EFFECT OF THE NUMBER OF FREQUENCY SAMPLES

The number of frequency samples  $N_f$  acquired from the VNA represents a trade-off between measurement time and quality of the acquisition. The higher  $N_f$  is, the longer the measurement takes, but the better the reconstruction is. From the results illustrated in Fig. 20, the optimal number of frequency samples is  $N_f = 101$ , which is the value assigned for the rest of the measurements. Below 51 samples (blue and red curves), the antenna pattern starts to degrade, appearing a ripple in the main lobe and losing the information of the first null. Below 13 samples (green curve), the ripple maintains and the symmetry in the main lobe is lost.

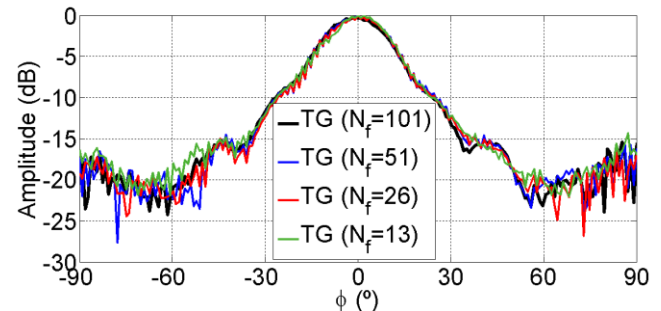


**FIGURE 20.** Effect of varying the number of frequency samples  $N_f$  obtained from the VNA. In all curves, a Hann window was used with  $t_1 = t_2 = t_{TG} = 2.2$  ns (20%).

### APPENDIX B. RECREATION OF THE MIMO SCENARIO

Fig. 21 describes in detail the recreation of the MIMO system shown in Fig. 6. As previously discussed in the text, a reference signal  $h_{ref}(t)$ , obtained from the measurement of a simple SISO (single input single output) scenario, is used to recreate the full MIMO system. Thus, each signal  $h_{ij}(t)$  that radiates the transmitter antenna  $TX_i$  and reaches the receiver antenna  $RX_j$  is an attenuated and delayed version of the reference signal  $h_{ref}(t)$ . That is,

$$h_{ij}(t) = A_{ij} h_{ref}(t - t_{ij}) \quad (3)$$

where  $A_{ij}$  is the attenuation factor and  $t_d$  is the time delay. Equivalently, the problem can be formulated in the frequency domain:

$$H_{ij}(f) = A_{ij} H_{\text{ref}}(f) e^{-j2\pi f t_{ij}} \quad (4)$$

where  $H_{\text{ref}}(f)$  is the Fourier transform of  $h_{\text{ref}}(t)$ .

By applying basic trigonometry, the time delay can be extracted from the location of the reference antennas. In Fig. 6, the reference antennas are TX<sub>1</sub> and RX<sub>2</sub> and their separation is  $d_{\text{ref}} = 80$  cm. Thus, the time delay is calculated as

$$t_{ij} = \frac{d_{ij} - d_{\text{ref}}}{c} \quad (5)$$

where  $c$  is the speed of light in the air. The attenuation factor  $A_{ij}$  is expressed as

$$A_{ij}[\text{dB}] = 0 - 20 \log(d_{ij}/d_{\text{ref}}) - \Delta G(\phi_{ij}) \quad (6)$$

$A_{ij}$  presents two major contributions: free space loss and a gain drop  $\Delta G(\phi_{ij})$  that depends on the position of RX antennas. Considering a normalized reference signal  $h_{\text{ref}}(t)$ , the term associated to free space loss is calculated with basic trigonometry, as shown in equation (6). The gain drop  $\Delta G(\phi_{ij})$  can be estimated by looking at the radiation pattern of the utilized horn antenna, displayed in Fig. 22. Note that if TX and RX antennas are aligned along the  $y$  axis ( $\phi_{ij} = 0$ ), the gain drop is zero.

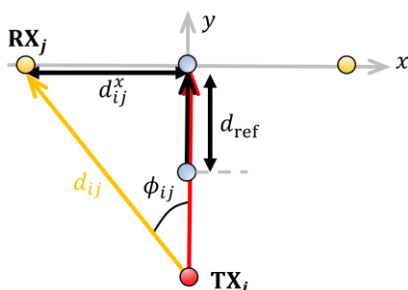


FIGURE 21. Recreation of the MIMO scenario for a pair of TX and RX antennas: TX<sub>i</sub> and RX<sub>j</sub>, respectively.

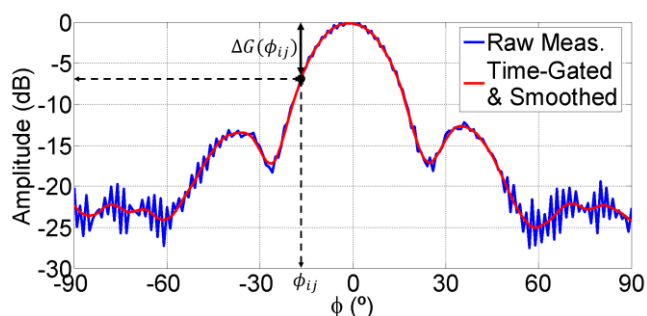


FIGURE 22. Measured and time-gated radiation pattern (E-plane) at 39 GHz of the horn antenna used in Section III. For a given azimuth angle  $\phi_{ij}$ , the gain drop can be estimated.

TABLE II  
ATTENUATION FACTORS AND TIME DELAYS OF THE MIMO 4X3 SCENARIO

	TX <sub>1</sub>	TX <sub>2</sub>	TX <sub>3</sub>	TX <sub>4</sub>
RX <sub>1</sub>	$\begin{pmatrix} 0.025 \\ (0.31 \text{ ns}) \end{pmatrix}$	$\begin{pmatrix} 0.056 \\ (1.23 \text{ ns}) \end{pmatrix}$	$\begin{pmatrix} 0.13 \\ (2.19 \text{ ns}) \end{pmatrix}$	$\begin{pmatrix} 0.20 \\ (3.15 \text{ ns}) \end{pmatrix}$
RX <sub>2</sub>	REF	$\begin{pmatrix} 0.76 \\ (1 \text{ ns}) \end{pmatrix}$	$\begin{pmatrix} 0.58 \\ (2 \text{ ns}) \end{pmatrix}$	$\begin{pmatrix} 0.52 \\ (3 \text{ ns}) \end{pmatrix}$
RX <sub>3</sub>	$\begin{pmatrix} 0.025 \\ (0.31 \text{ ns}) \end{pmatrix}$	$\begin{pmatrix} 0.056 \\ (1.23 \text{ ns}) \end{pmatrix}$	$\begin{pmatrix} 0.13 \\ (2.19 \text{ ns}) \end{pmatrix}$	$\begin{pmatrix} 0.20 \\ (3.15 \text{ ns}) \end{pmatrix}$

The different attenuation factors and time delays used for the reconstruction of the MIMO 4x3 scenario presented in Section III.B are illustrated in Table II. For each cell of Table II, the attenuation factor (in linear units) is shown at the top and the time delay at the bottom. The reference is assumed to present no attenuation ( $A_{12} = 1$ ) and no delay ( $t_{12} = 0$ ). The incoming signals to RX<sub>1</sub> and RX<sub>3</sub> can be considered the same in practice, since the radiation pattern of the TX antenna is symmetric and both antennas are separated 40 cm from the central receiver, RX<sub>2</sub>. Therefore, RX<sub>1</sub> and RX<sub>3</sub> share identical attenuation factors and delays.

## ACKNOWLEDGMENT

The authors would like to thank M. Bolívar-Lupiáñez and A. Gutiérrez-Martínez for their help in preparing the measurement set-up and in the acquisition and processing of some experimental results.

## REFERENCES

- [1] Ericsson, "Ericsson Mobility Report November 2019," 2019. [Online]. Available: <https://www.ericsson.com/4acd7e/assets/local/mobility-report/documents/2019/emr-november-2019.pdf>
- [2] W. D. de Mattos and P. R. L. Gondim, "M-Health Solutions Using 5G Networks and M2M Communications," *IT Professional*, vol. 18, no. 3, pp. 24-29, May-June 2016.
- [3] S. Mattisson, "An Overview of 5G Requirements and Future Wireless Networks: Accommodating Scaling Technology," *IEEE Solid-State Circuits Magazine*, vol. 10, no. 3, pp. 54-60, Summer 2018.
- [4] A. Ghosh, A. Maeder, M. Baker and D. Chandramouli, "5G Evolution: A View on 5G Cellular Technology Beyond 3GPP Release 15," *IEEE Access*, vol. 7, pp. 127639-127651, 2019.
- [5] R. Lu, L. Zhang, J. Ni and Y. Fang, "5G Vehicle-to-Everything Services: Gearing Up for Security and Privacy," *Proceedings of the IEEE*, vol. 108, no. 2, pp. 373-389, Feb. 2020.
- [6] M. A. Khan, N. Saeed, A. W. Ahmad and C. Lee, "Location Awareness in 5G Networks Using RSS Measurements for Public Safety Applications," *IEEE Access*, vol. 5, pp. 21753-21762, 2017.
- [7] Release 17 from 3GPP [Online]. Available: <https://www.3gpp.org/release-17>
- [8] 5GCM, "5G channel model for bands up to 100 GHz," Technical Report, Oct.2016. [Online]. Available: <http://www.5gworkshops.com/5GCM.html>.
- [9] K. Haneda et al., "5G 3GPP-Like Channel Models for Outdoor Urban Microcellular and Macrocellular Environments," in *IEEE 83rd Vehicular Technology Conference (VTC Spring)*, Nanjing, 2016, pp. 1-7.

- [10] N. Zhang et al., "Dynamic Channel Modeling for an Indoor Scenario at 23.5 GHz," *IEEE Access*, vol. 3, pp. 2950-2958, 2015.
- [11] I. Rodríguez, H. C. Nguyen, I. Z. Kovács, T. B. Sørensen and P. Mogensen, "An Empirical Outdoor-to-Indoor Path Loss Model From Below 6 GHz to cm-Wave Frequency Bands," *IEEE Antennas and Wireless Propagation Letters*, vol. 16, pp. 1329-1332, 2017.
- [12] J. Du, D. Chizhik, R. Feick, G. Castro, M. Rodríguez and R. A. Valenzuela, "Suburban Residential Building Penetration Loss at 28 GHz for Fixed Wireless Access," *IEEE Wireless Communications Letters*, vol. 7, no. 6, pp. 890-893, Dec. 2018.
- [13] T. Zhou, H. Li, Y. Wang, L. Liu and C. Tao, "Channel Modeling for Future High-Speed Railway Communication Systems: A Survey," *IEEE Access*, vol. 7, pp. 52818-52826, 2019.
- [14] C. Briso-Rodríguez, P. Fratilesco and Y. Xu, "Path Loss Modeling for Train-to-Train Communications in Subway Tunnels at 900/2400 MHz," *IEEE Antennas and Wireless Propagation Letters*, vol. 18, no. 6, pp. 1164-1168, June 2019.
- [15] C. Wang, J. Bian, J. Sun, W. Zhang and M. Zhang, "A Survey of 5G Channel Measurements and Models," *IEEE Communications Surveys & Tutorials*, vol. 20, no. 4, pp. 3142-3168, Fourthquarter 2018.
- [16] I. A. Hemadeh, K. Satyanarayana, M. El-Hajjar and L. Hanzo, "Millimeter-Wave Communications: Physical Channel Models, Design Considerations, Antenna Constructions, and Link-Budget," *IEEE Communications Surveys & Tutorials*, vol. 20, no. 2, pp. 870-913, Secondquarter 2018.
- [17] W. Khawaja, I. Guvenc, D. W. Matolak, U. Fiebig and N. Schneckenburger, "A Survey of Air-to-Ground Propagation Channel Modeling for Unmanned Aerial Vehicles," *IEEE Communications Surveys & Tutorials*, vol. 21, no. 3, pp. 2361-2391, thirdquarter 2019.
- [18] G. Ferrara, M. Migliaccio and A. Sorrentino, "Characterization of GSM Non-Line-of-Sight Propagation Channels Generated in a Reverberating Chamber by Using Bit Error Rates," *IEEE Transactions on Electromagnetic Compatibility*, vol. 49, no. 3, pp. 467-473, Aug. 2007.
- [19] S. Herbert, I. Wassell, T. Loh and J. Rigelsford, "Characterizing the Spectral Properties and Time Variation of the In-Vehicle Wireless Communication Channel," *IEEE Transactions on Communications*, vol. 62, no. 7, pp. 2390-2399, July 2014.
- [20] L. Gagliardi, D. Micheli, G. Gradoni, F. Moglie and V. M. Primiani, "Coupling Between Multipath Environments Through a Large Aperture," *IEEE Antennas and Wireless Propagation Letters*, vol. 14, pp. 1463-1466, 2015.
- [21] A. K. Fall, P. Besnier, C. Lemoine, M. Zhadobov and R. Sauleau, "Design and Experimental Validation of a Mode-Stirred Reverberation Chamber at Millimeter Waves," *IEEE Transactions on Electromagnetic Compatibility*, vol. 57, no. 1, pp. 12-21, Feb. 2015.
- [22] M. Barazzetta et al., "A Comparison Between Different Reception Diversity Schemes of a 4G-LTE Base Station in Reverberation Chamber: A Deployment in a Live Cellular Network," *IEEE Transactions on Electromagnetic Compatibility*, vol. 59, no. 6, pp. 2029-2037, Dec. 2017.
- [23] X. Chen et al., "Reverberation Chambers for Over-the-Air Tests: An Overview of Two Decades of Research," *IEEE Access*, vol. 6, pp. 49129-49143, 2018.
- [24] E. Genender, C. L. Holloway, K. A. Remley, J. M. Ladbury, G. Koepke and H. Garbe, "Simulating the Multipath Channel With a Reverberation Chamber: Application to Bit Error Rate Measurements," in *IEEE Transactions on Electromagnetic Compatibility*, vol. 52, no. 4, pp. 766-777, Nov. 2010.
- [25] J.F. Valenzuela-Valdés, A.M. Martínez-González and D.A. Sánchez-Hernández "Emulation of MIMO nonisotropic fading environments with reverberation chambers," *IEEE Antennas and Wireless Propagation Letters*, vol. 7, pp. 325 – 328, 2008.
- [26] J.F. Valenzuela-Valdés, A.M. Martínez-González and D.A. Sánchez-Hernández, "Diversity gain and MIMO capacity for nonisotropic environments using a reverberation chamber," *IEEE Antennas and Wireless Propagation Letters*, vol. 8, pp. 112 – 115, 2009.
- [27] M. S. Kildal, J. Carlsson and A. Alayón Glazunov, "Measurements and Simulations for Validation of the Random-LOS Measurement Accuracy for Vehicular OTA Applications," *IEEE Transactions on Antennas and Propagation*, vol. 66, no. 11, pp. 6291-6299, Nov. 2018.
- [28] D. Solomitckii et al., "Characterizing Radio Wave Propagation in Urban Street Canyon With Vehicular Blockage at 28 GHz," *IEEE Transactions on Vehicular Technology*, vol. 69, no. 2, pp. 1227-1236, Feb. 2020.
- [29] J.D. Sánchez-Heredia, J.F. Valenzuela-Valdés, A.M. Martínez-González and D.A. Sánchez-Hernández, "Emulation of MIMO rician-fading environments with mode-stirred reverberation chambers," *IEEE Transactions on Antennas and Propagation*, vol. 59, no. 2, pp. 654 – 660, 2011.
- [30] J.D. Sánchez-Heredia, M. Grudén, J.F. Valenzuela-Valdés and D.A. Sánchez-Hernández, "Sample-selection method for arbitrary fading emulation using mode-stirred chambers," *IEEE Antennas and Wireless Propagation Letters*, vol. 9, pp. 409 – 412, 2010.
- [31] O. Zetterstrom, E. Pucci, P. Padilla, L. Wang, and O. Quevedo-Teruel, "Low-Dispersive Leaky-Wave Antennas for mmWave Point-to-Point High-Throughput Communications," *IEEE Transactions on Antennas and Propagation*, vol. 68, no. 3, pp. 1322-1331, 2019.
- [32] Q. Chen, O. Zetterstrom, E. Pucci, A. Palomares-Caballero and P. Padilla, "Glide-Symmetric Holey Leaky-Wave Antenna with Low Dispersion for 60-GHz Point-to-Point Communications," *IEEE Transactions on Antennas and Propagation*, vol. 68, no. 3, pp. 1925-1936, 2019.
- [33] A. Palomares-Caballero, A. Alex-Amor, J.F. Valenzuela-Valdés and Pablo Padilla, "Millimeter-Wave 3D-Printed Antenna Array based on Gap-Waveguide Technology and Split E-plane Waveguide," *IEEE Transactions on Antennas and Propagation*, in early access, 2020
- [34] J. Koh, A. De, T. K. Sarkar, H. Moon, W. Zhao and M. Salazar-Palma, "Free Space Radiation Pattern Reconstruction from Non-Anechoic Measurements Using an Impulse Response of the Environment," *IEEE Trans. Antenna Propag.*, vol. 60, no. 2, pp. 821-831, Feb. 2012.
- [35] A. Soltane, G. Andrieu, E. Perrin, C. Decroze and A. Reineix, "Antenna Radiation Pattern Measurement in a Reverberating Enclosure Using the Time-Gating Technique," *IEEE Antennas Propag. Lett.*, vol. 19, no. 1, pp. 183-187, Jan. 2020.
- [36] T. L. Marzetta, E. G. Larsson, H. Yang and H. Q. Ngo, *Fundamentals of Massive MIMO*. Cambridge, United Kingdom: Cambridge University Press, 2018.
- [37] S. Loyka and G. Levin, "On physically-based normalization of MIMO channel matrices," *IEEE Trans. Wireless Commun.*, vol. 8, no. 3, pp. 1107-1112, March 2009.
- [38] M. A. Jensen and J. W. Wallace, "A review of antennas and propagation for MIMO wireless communications," *IEEE Trans. Antennas Propag.*, vol. 52, no. 11, pp. 2810-2824, Nov. 2004.
- [39] P.-S. Kildal and K. Rosengren, "Correlation and capacity of MIMO systems and mutual coupling, radiation efficiency, and diversity gain of their antennas: simulations and measurements in a reverberation chamber," *IEEE Commun. Mag.*, vol. 42, no. 12, pp. 104-112, Dec. 2004.
- [40] LEHA Laboratory of the Technical University of Madrid [Online]. Available: <https://www.gr.ssr.upm.es/index.php/en/leha/about-us>
- [41] Z. Chen and Z. Xiong, "Differences of Time Domain Gating Implementations in Vector Network Analyzers," in *Joint International Symposium on Electromagnetic Compatibility, Sapporo and Asia-Pacific International Symposium on Electromagnetic Compatibility (EMC Sapporo/APEMC)*, Sapporo, Japan, 2019, pp. 597-600.



**ALEJANDRO RAMIREZ-ARROYO** was born in Córdoba, Spain, in 1997. He received the B.Sc. degree in Telecommunication Engineering from the University of Granada, Spain, in 2019, where he is currently pursuing the M.Sc. degree in Telecommunication Engineering. His current research interests include heterogeneous networks, optimization techniques and propagation channels and models for 5G networks.



**ANTONIO ALEX-AMOR** received the B.Sc. degree in telecommunication engineering from Universidad de Granada, in 2016, and the M.Sc. degree in telecommunication engineering from Universidad Politécnica de Madrid (UPM), in 2018, where he is currently pursuing the Ph.D. degree. Since 2016, he has been with the Radiation Group, Signal, Systems and Radiocommunications Department, UPM. From 2018-2019, he joined the Department of Language and Computer Science, Universidad de Malaga. In 2020, he joined the Signal Theory, Telematics and Communications Department, University of Granada. He received the Best Electromagnetics Paper Award at the 14th European Conference on Antennas and Propagation (EuCAP 2020). His current research interests include the use of liquid crystal as tunable dielectric, metamaterials, structures with higher symmetries and radiofrequency energy harvesting systems.



networks.

**CARMELO GARCÍA-GARCÍA** was born in Sanlúcar de Barrameda, Spain, in 1996. In 2019, he received the BSc in Telecommunication Engineering from the University of Seville (US), Seville, Spain, and he is currently studying an MSc in Telecommunication Engineering at the University of Granada (UGR), Granada, Spain. His current research interests include electromagnetic compatibility (EMC) and optimization techniques for 5G



antennas and phase shifters, gap-waveguide, structures with higher symmetries and optimization algorithms.

**ANGEL PALOMARES-CABALLERO** was born in 1994 in Jaen, Spain. He received his B.Sc. and M.Sc. in Telecommunication Engineering from the University of Granada (UGR), Spain, in 2016 and 2018, respectively. Since 2017, he has been in the Department of Signal Theory, Telematics and Communications of University of Granada, where he is currently a Ph.D student with a national predoctoral fellowship. His research interests include millimeter-wave



**PABLO PADILLA** was born in Jaen, Spain, in 1982. He received the Telecommunication Engineering degree and the Ph.D. degree from the Radiation Group (Signal, Systems and Radiocommunications Department) of the Technical University of Madrid (UPM), Spain, in 2005 and 2009, respectively. In 2007, he was with the Laboratory of Electromagnetics and Acoustics, Ecole Polytechnique Fédérale de Lausanne, Switzerland, as an invited Ph.D. Student. In 2009, he carried out a Postdoctoral stay at the Helsinki University of Technology (AALTO-TKK). In 2009, he became Assistant Professor at the Signal Theory, Telematics and Communications Department of the University of Granada, where he is currently Associate Professor, since 2012. In 2017, he was an invited Visiting Professor at the Royal Institute of Technology of Stockholm. He has authored more than 65 high-impact journal contributions and more than 60 contributions to international symposia. His research interests include a variety of topics related mainly to electromagnetism and communication issues (radiofrequency devices, antennas and propagation).



**JUAN VALENZUELA-VALDES** was born in Marbella, Spain. He received the degree in telecommunications engineering from the Universidad de Malaga, Spain, in 2003, and the Ph.D. degree from the Universidad Politécnica de Cartagena, Spain, in 2008, where he joined the Department of Information Technologies and Communications, in 2004. In 2007, he joined EMITE Ing. as the Head of research. In 2011, he joined the Universidad de Extremadura, and in 2015, he joined the Universidad de Granada, where he is currently an Associate Professor. He has also received several prizes, including a National Prize to the Best Ph.D. in Mobile Communications by Vodafone. He also holds several national and international patents. His publication record comprised of more than 100 publications, including 50 JCR indexed articles and seven book chapters. (Updated March 2019). His current research interests include wireless communications, radiofrequency devices, antennas and propagation. He is the head of SWAT research group (<https://swat.ugr.es/>) at the University of Granada and cohead of Singular Laboratory of Electromagnetic characterization of microwave and millimeter devices and antennas.